C. R. Mecanique 345 (2017) 779–796

Contents lists available at ScienceDirect

Comptes Rendus Mecanique

www.sciencedirect.com

DEM analysis of the effect of joint geometry on the shear behavior of rocks

Mingjing Jiang [a,b,c,*], Jun Liu [b,c], Giovanni B. Crosta [d], Tao Li [b,c]

[a] State Key Laboratory for Disaster Reduction in Civil Engineering, Tongji University, Shanghai, 200092, China
[b] Key Laboratory of Geotechnical and Underground Engineering of Ministry of Education, Tongji University, Shanghai, 200092, China
[c] Department of Geotechnical Engineering, College of Civil Engineering, Tongji University, Shanghai, 200092, China
[d] Department of Earth and Environmental Sciences, Università degli Studi di Milano–Bicocca, Milano, Italy

ARTICLE INFO

Article history:
Received 15 February 2017
Accepted 13 July 2017
Available online 18 August 2017

Keywords:
Rock joints
Distinct element method
Particle bonding
Joint geometries
Direct shear test

ABSTRACT

In order to comprehensively investigate the effect of different joint geometries on the shear behavior of rocks, the Distinct Element Method (DEM) was utilized with a new bond contact model. A series of direct shear tests on coplanar and non-coplanar jointed rocks was simulated using the PFC2D software, which incorporates our bond contact model. Both coplanar jointed rocks with different joint persistence and non-coplanar ones with different joint inclinations were simulated and investigated numerically. The numerical results were compared and discussed with relevant laboratory tests as well as some reported numerical works. The results show that for coplanar jointed rocks, the peak shear stress decreases nonlinearly with the joint persistence, and the failure process can be divided into four stages: elastic shearing phase, crack propagation, failure of rock bridges, and residual phase. For non-coplanar jointed rocks, as the absolute value of the inclination angle of the rock joints increases, its shear strength increases, changing the failure patterns and the length of new fractures between existing cracks. When the absolute value increases from 15° to 30°, the average shear capacity increases the most as 39%, while the shear capacity increases the least as 2.9% when the absolute value changes from 45° to 60°. There is a good consistency of the failure patterns obtained from experiments and numerical tests. All these demonstrate that the DEM can be further applied to rock mechanics and practical rock engineering with confidence in the future.

1. Introduction

The behavior of a rock mass is determined not only by the properties of the rock matrix, but also by the presence and properties of rock joints. The initiation, propagation and coalescence of rock joints are important factors in controlling the mechanical behavior of rocks [1–4], and comprehensive analysis of the joints failure behavior facilitates a better understanding of the failure mechanism of rocks.

Various methods have been employed to analyze the failure mechanism of rock joints such as laboratory tests and numerical simulations. In laboratory tests, direct shear tests are often utilized to investigate the shear properties of jointed

* Corresponding author at: Department of Geotechnical Engineering, College of Civil Engineering, Tongji University, Shanghai, 200092, China.
E-mail address: mingjing.jiang@tongji.edu.cn (M.J. Jiang).

http://dx.doi.org/10.1016/j.crme.2017.07.004
1631-0721/

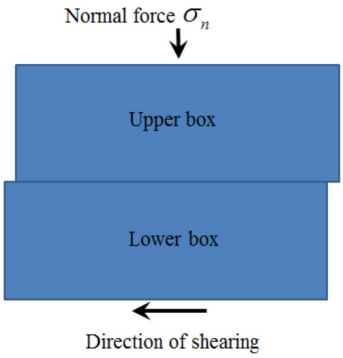

Fig. 1. Schematic of the direct shear test.

rocks. In the direct shear test, shearing of the sample is achieved by pushing the lower shear box horizontally while the upper shear box is restrained with a given normal force applied vertically, as illustrated in Fig. 1. Pioneering work done by Lajtai [5,6] revealed that tensile wing cracks first appear at the tips of the horizontal joints, followed by the secondary shear cracks propagating towards the opposite joints. Gehle and Kutter [7] argued that the failure pattern and the shear resistance of jointed rock are significantly affected by the orientation of the joints and the normal stress. Wong et al. [8] studied the shear strength and failure patterns of artificial rock-like models containing open non-persistent joints, and the results showed that the failure pattern was controlled by both the normal stress and the joint separation. More recently, Cao et al. [9] found that the rock specimen takes a turn from wing crack propagation failure to crack coalescence failure with the increase in the rock bridge angle. Moradian [10] carried out a series of uniaxial compression tests on granite specimens containing pre-existing flaws and monitored the cracking process by acoustic emission and high-speed video imaging. The results showed that the classification of cracking levels contains eight stages.

As experimental results are very sensitive to sample preparation techniques and boundary loading conditions, and some important microscopic information controlling the failure patterns still remains unknown, many researchers turned to numerical methods in studying the shear behavior of rock joints, including the continuum [11,12] and discontinuum medium method [3,13,14]. Among these methods, the Distinct Element Method (DEM) proposed by Cundall and Strack [15] is a feasible method to study the shear behavior and failure mechanism of rocks. This method is based on the discrete mechanics and treats rocks and soils as assemblies of discrete elements, whose movements are determined by interparticle contact forces and the Newtonian second law. A large number of DEM simulation works have been done by researchers to investigate the shear behavior of rocks. Potyondy and Cundall [16] proposed the bonded particle model (BPM) to reproduce the main mechanical behavior of Lac du Bonnet granite in DEM uniaxial and triaxial tests. Cho et al. [17] developed a new clumped-particle model to predict the strength of the synthetic rock independent of stress path. Wang and Tonon [18] developed a DEM code to model Lac du Bonnet granite behavior in triaxial compression tests till failure. The results showed that the microlevel tensile failures occur first, followed by mobilization of residual friction. Three distinct stages of a stress–strain curve can be identified. Yang et al. [19] performed DEM simulation on the fracture coalescence behavior of red sandstone specimen containing two unparallel fissures under uniaxial compression using PFC2D. The mechanical parameters were investigated systematically by comparing the numerical results with their experimental data [20]. Based on BPM, Zhang et al. [21,22] systemically studied crack initiation, propagation and coalescence in a rock-like material with a single or two flaws. However, the bond contact models used by most researchers in their DEM simulations are necessarily hypothesized with inadequate experimental verification. Although the DEM is free from the restriction of complex constitutive models, the reliability of the DEM simulations is susceptible to the contact model which defines the contact logic connecting the basic elements. Based on a series of experiments on bonded granules idealized by two glued aluminum rods, Jiang et al. [23] developed a novel bond contact model, which was implemented into a two-dimensional (2D) DEM code and was calibrated by comparing a series of numerical results with available experimental data. This new bond contact model was proven to be able to capture the main mechanical behaviors of crystalline rocks (Lac du Bonnet granite) and to simulate crack propagation and rock fracture in rock samples containing single and double flaws [23], which constitutes the reason for employing the model in this paper.

Previous works have promoted the understanding of failure behavior of jointed rocks. Nevertheless, most of them focused on analyzing rocks with one given joint type or failure of the rock joints with simple geometrical orientation. To investigate the effect of different joint geometries on the shear behavior of jointed rocks comprehensively, this paper simulated a series of direct shear tests on coplanar and non-coplanar jointed rocks using the PFC2D incorporating the new bond contact model. The bond contact model is introduced firstly, and then the DEM with the calibrated bond contact model is used to simulate a series of direct shear tests on jointed rocks, of which the effects of joint persistence and joint inclinations are analyzed. After that, the DEM results are compared with the available experimental data in terms of shear curve, bond breakage, failure pattern, and shear capacity. It is the authors' opinion that the DEM can be applied to rock mechanics and rock engineering in the future only after the DEM can well capture the main features of the real rock observed experimentally.

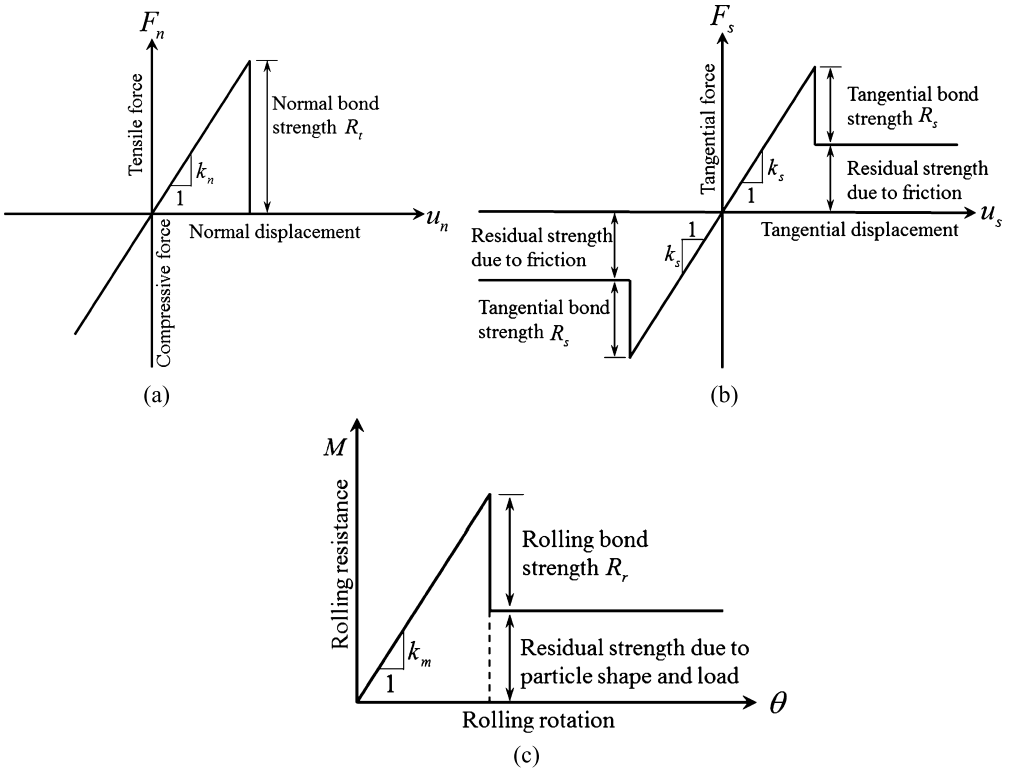

Fig. 2. Mechanical response of the bond contact model: (a) normal mechanical response; (b) tangential mechanical response; and (c) rolling mechanical response.

2. The bond contact model

The bond contact model used in this paper was developed on the basis of experimental investigation and theoretical analysis. This part gives a brief description of the contact model and more detailed information can be found in reference [23]. The contact model is derived by a series of laboratory tests on a pair of aluminum rods glued together by a rock-like material, i.e. cement. Five different types of tests, i.e. tension, compression, shear, rolling and shear–rolling under different normal forces, were designed to characterize the mechanical behavior of the cemented samples [24,25]. Based on these tests, the mechanical responses of the model were verified and the strength envelopes were obtained [23].

2.1. Mechanical response

The mechanical response of the bond contact model was deduced firstly through reasonable theoretical derivation [26,27], and then it was established and verified by a series of laboratory tests on cemented granules [24,25]. Contact forces are assumed to be transferred through the bond and particles in contact:

$$F_{\mathrm{n}} = F_{\mathrm{nb}} + F_{\mathrm{np}}, \qquad F_{\mathrm{s}} = F_{\mathrm{sb}} + F_{\mathrm{sp}}, \qquad M = M_{\mathrm{b}} + M_{\mathrm{p}} \tag{1}$$

where F_{n}, F_{s} and M are the normal force, shear force and moment, respectively; and F_{nb}, F_{sb} and M_{b} are the normal force, the shear force and the moment transferred through the bond, respectively, with subscript "b" standing for "bond", while F_{np}, F_{sp} and M_{p} are the corresponding components transferred through the particles in contact, with subscript "p" standing for "particle".

Fig. 2(a) presents the normal mechanical response. In tension, the normal contact force F_{n} between two particles is a product of the normal stiffness coefficient k_{n} and tension displacement u_{n} before its value reaches the normal bond strength R_{t}. When the force arrives at the normal bond strength R_{t}, the bond is broken, and the normal force abruptly reduces to zero. In compression, the contact force is always a product of k_{n} and of a compression displacement, u_{n}. Fig. 2(b) presents the tangential force–displacement relationship. The shear force increases linearly with the increasing of tangential displacement u_{s} up to the shear strength, R_{s}. After the peak value is reached, the bond breaks and the tangential force drops to the residual frictional shear strength, R_{sr}. In Fig. 2(c), the mechanical response in the rolling contact's direction is similar to that in the tangential direction; namely, the moment M is a product of the rolling stiffness, k_{m}, and the relative rolling rotation θ, and after the bond's failure, it drops to the residual strength, R_{rr}, which is influenced by the particle's shape.

2.2. Strength envelope

In nature, the contact thickness between mineral grains is so small that the central thickness of two neighboring mineral grains can be regarded as zero. At this moment, the complete contact between two particles in this model is composed of both an interparticle contact and an inter-bond contact, and they transmit the applied normal compression force F_n in a parallel mode.

The shear strength is contributed by the bond strength and the interparticle strength when the normal force is compressive. Therefore, the shear strength R_s and rolling strength R_r can be expressed respectively by:

$$R_s = \mu_b f R_c \left[1 + g_s \left(\ln \frac{1}{f}\right)^{f_s}\right] + \mu_p F_{np} \tag{2}$$

$$R_r = \frac{1}{6}\beta_b \bar{r} f R_c \left[1 + g_r \left(\ln \frac{1}{f}\right)^{f_r}\right] + \frac{1}{6}\beta_p \bar{r} F_{np} \tag{3}$$

where $f = (F_n + R_t)/(R_t + R_c)$ is the stress ratio; R_c is the compressive strength and R_t is the tensile strength; μ_b and μ_p are friction coefficients of the bonds and the particles, respectively; g_s and g_r determine the percentage of the bond part; f_s and f_r control the envelope shapes; $\bar{r} = 2r_1 r_2/(r_1 + r_2)$ is the common radius of the two contacted particles, whose radii are r_1 and r_2, respectively; β_p and β_b are the particle rolling resistance coefficients and the rolling resistance coefficients of the bonds, respectively.

Correspondingly, the residual shear strength R_{sr}, the rolling strength R_{rr}, and the critical normal force R_{cbr} can be expressed respectively by:

$$R_{sr} = \mu_b F_{nb} + \mu_p F_{np} \tag{4}$$

$$R_{rr} = \frac{1}{6}\beta_b \bar{r} F_{nb} + \frac{1}{6}\beta_p \bar{r} F_{np} \tag{5}$$

$$R_{cbr} = \frac{k_{nb} + k_{np}}{k_{nb}} R_c \tag{6}$$

When the normal force F_n is compressive, but less than the critical normal force R_{cbr}, both the interparticle friction and bond strength contribute to the peak shear and rolling strength, which are predicted respectively by Eqs. (2) and (3). The bond breaks if its peak strength has arrived, and the shear and rolling resistance decrease to their residual values predicted respectively by Eqs. (4) and (5).

In the case where the normal force F_n is compressive and larger than the critical normal force R_{cbr}, the bond is broken, and the peak strength envelopes are coincident with residual strength envelopes, which are expressed by Eqs. (4) and (5).

When the normal force F_n is tensile, the peak strength is completely dependent on the bond's strength. The peak shear and rolling strength envelopes at this stage are expressed by the first item on the right-hand side in Eqs. (2) and (3).

2.3. Calibration of the model parameters

To calibrate the parameters of the model, a series of numerical simulations were carried out by adjusting the microscopic parameters (i.e. the parameters of the contact model) until the mechanical properties obtained are consistent with the experimental data published in references [28,29]. In this work, Lac du Bonnet granite is chosen as the target material for the DEM simulations. At the beginning of these numerical tests, homogeneous samples were generated by the Multi-Layer with Undercompaction Method [30], with maximum, minimum and average grain diameters being 2.0, 0.5, and 1.3 mm, respectively. The uniformity coefficient and curvature coefficient are 2.4 and 1.1, respectively. The initial planar void ratio 0.2 is chosen as a representative value for a dense sample. After the intact rock sample was generated, direct tension test, Brazilian test and uniaxial compression test were simulated for calibration. The values of the fitting parameters f_s, g_s, f_r, and g_r obtained by matching the experimental data [23] are 0.986, 2.15, 0.761 and 3.055, respectively.

The bond tensile strength, R_{bt}, was firstly calibrated via simulating direct tension tests. The numerical results revealed that the rock tensile strength σ_t increases linearly with R_{bt}, and the value of R_{bt} was calibrated as a value of $6.5 \cdot 10^4$ N to produce a direct tensile strength of 8.7 MPa, which is the value obtained previously from the experiments [28]. Then, a Brazilian test was numerically simulated in order to validate the obtained R_{bt}. The simulated Brazilian tensile strength is 10.4 MPa, and is very close to the value of 10 MPa measured in the laboratory [28]. The peak stress obtained from the experiments [28] and DEM tests are in good agreement, as illustrated in Fig. 3. After R_{bt} was determined, uniaxial compression tests were simulated to calibrate other model parameters. For a given stiffness ratio (k_s/k_n), Young's modulus E increases linearly with the normal stiffness k_n, and the Poisson ratio ν is only related to the ratio k_s/k_n. Different combinations of k_n and k_s/k_n were employed in the simulation of uniaxial compression tests, and the numerical results were compared with the published data on Lac du Bonnet granite. The calibrated values of k_n and k_s are $1.8 \cdot 10^{11}$ N/m and $9.47.5 \cdot 10^{10}$ N/m, respectively, and they result in simulated macroscopic deformability properties $E = 67.53$ GPa and $\nu = 0.256$, which are very close to the average experimental values of $E = 69$ GPa and $\nu = 0.26$ [28,29]. The rock compressive strength σ_c increases

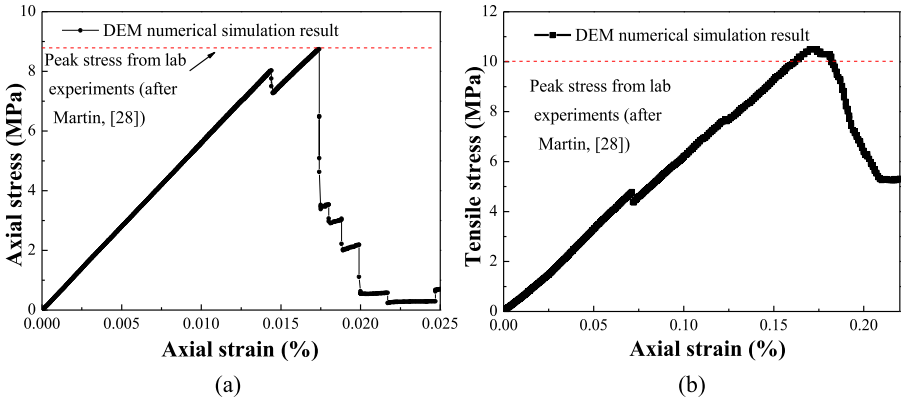

Fig. 3. Comparison between DEM simulation and experiments [28]: (a) direct tension test and (b) Brazilian tension test.

Table 1
Particle and bond parameters of the DEM model.

Parameters	Value for intact rock	Value for joint
Particle density ρ_s (kg/m^3)	2700	2700
Planar void ratio e	0.20	0.20
Normal stiffness of particles k_{np} (N/m)	$1.8 \cdot 10^{11}$	$1.8 \cdot 10^{11}$
Tangential stiffness of particles k_{sp} (N/m)	$9.47 \cdot 10^{10}$	$9.47 \cdot 10^{10}$
Normal stiffness of bonds k_{nb} (N/m)	$9.0 \cdot 10^{10}$	$9.0 \cdot 10^{10}$
Tangential stiffness of bonds k_{sb} (N/m)	$4.735 \cdot 10^{10}$	$4.735 \cdot 10^{10}$
Tensile strength of bonds R_t (N)	$6.5 \cdot 10^{4}$	0.0
Compressive strength of bonds R_c (N)	$8.0 \cdot 10^{7}$	0.0
Interparticle friction coefficient μ_p	1.0	0.2
Interparticle rolling resistance coefficient β_p	1.5	0.0
Friction coefficient of bonds μ_b	0.5	0.1
Rolling resistance coefficient of bonds β_b	0.5	0.0
Fitting parameter f_s	0.986	0.986
Fitting parameter g_s	2.15	2.15
Fitting parameter f_r	0.761	0.761
Fitting parameter f_r	3.055	3.055

with R_c in a logarithmic mode, and R_c is set to be $8 \cdot 10^7$ N by calibration against experimental data [28,29]. The bond friction coefficient μ_b is set to be 0.5, since μ_b mainly affects the post-peak mechanical response, and there is no experimental value in reference [28]. Then, the interparticle friction coefficient $\mu_p = 1.0$ was selected based on the ratio of μ_p to μ_b obtained from the experiments on aluminum rods [24,25]. Our previous analyses demonstrated that the bond and interparticle rolling resistance coefficients (β_b and β_p) affect the crack propagation pattern [23]. In order to simulate the crack propagation observed by Wang and Mora [31], these two parameters were set to 0.5 and 1.5, respectively. Referring to [1,14], the strength parameters of bonds for the joint (R_{bt}, R_{bc}, β_p, and β_b) are set to be 0 for simplicity. μ_b and μ_p for the joint are chosen as 0.1 and 0.2, respectively, based on our experience. Other parameters for the joint are the same as those for the intact rock. Note that although the normal and tangential bond stiffness (k_{nb} and k_{sb}) of the joint have the same values as the particles ($9.47 \cdot 10^{10}$ N/m and $9.0 \cdot 10^{10}$ N/m respectively), the bond stiffness of the joint practically has no effect, since the bond of the joint has no strength.

The calibrated model parameters, as illustrated in Table 1, were used to carry out a series of simulations to demonstrate the performance of the DEM intact rock samples. In addition, the numerical results can be influenced by damping, as discussed in [32]. In this study, a local damping of 0.7 is used based on our previous analyses [23]. The strength envelopes obtained from the DEM biaxial compression tests and the laboratory tests on Lac du Bonnet granite [28] are presented in Fig. 4, which shows that the model is capable of reproducing the strength envelope of Lac du Bonnet granite at least up to medium values of confining stress. Note that compared with other DEM contact models, the contact model used in this study is established on experimental results [24,25]. Therefore, the benefits of this model are compelling, despite the fact that it is a little complex compared with some other contact models.

3. DEM direct shear tests on jointed rocks

3.1. Jointed rock sample

In order to generate a jointed rock sample, a rock sample containing 10,000 particles with size of 12.2 cm × 7.8 cm was generated at first with the same procedure as that mentioned in the previous section, as illustrated in Fig. 5. Then, joints

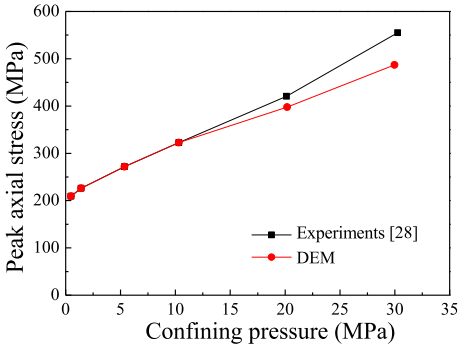

Fig. 4. Strength envelopes obtained from DEM simulations and experiments [28] on Lac du Bonnet granite.

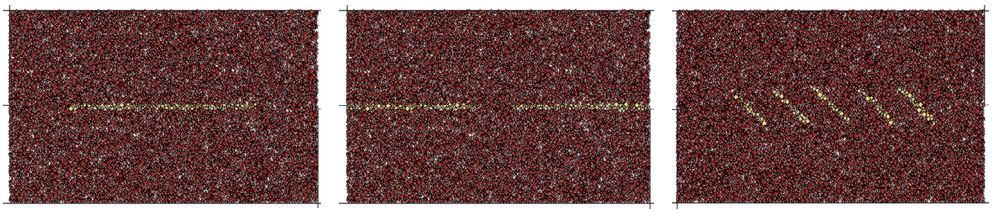

(a) Coplanar joint (mode I) (b) Coplanar joint (mode II) (c) Non-coplanar joint

Fig. 5. Geometry of the three types of numerical jointed rock samples (width: 12.2 cm; height: 7.8 cm).

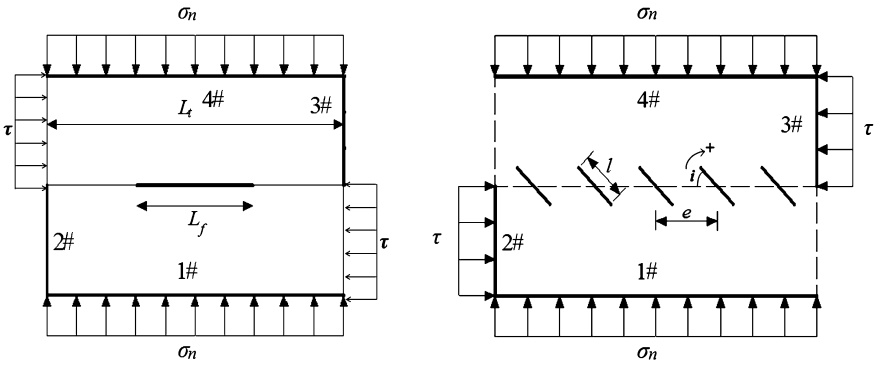

(a) Coplanar joint (b) Non-coplanar joint

Fig. 6. Settings of sample geometry and boundary conditions of the loading process for the simulated direct shear test.

(marked in yellow) were generated within the rectangular DEM sample. Herein joints are identified as layers of particles with a thickness of four times the minimum particle diameter. The microscopic contact properties shown in Table 1 are assigned to the contact for the particles forming the joint layers. The two-dimensional assemblage with rock joints is characterized by three geometrical parameters: the inclination angle, i (i.e. the angle between the joint and the negative direction of the horizontal axis, positive if the angle is clockwise), the length, l, and the distance between adjacent joints, e.

3.2. DEM simulation procedure

Fig. 6 illustrates the settings of the DEM direct shear test. Tests with different joint persistence k (i.e. the ratio of joint length, L_f, to the total length, L_t, of the shear plane) and joint inclination i are simulated and analyzed in this study. For a coplanar joint, the effect of joint persistence (i.e. 0.6, 0.8 and 0.9) was studied with a constant normal stress of 1 MPa. For a non-coplanar joint, the effect of joint inclination (i.e. 90°, 75°, 60°, 45°, 30°, 15°, 0°, −15°, −30°, −45°, −60°, and −75°) was investigated with a fixed normal stress of 1 MPa and a given parameter l/e of 0.8. An inherent purpose of choosing such parameters is to compare the numerical results with the experimental data [5–7,33] to verify the DEM before it can be further applied to rock mechanics and practical rock engineering. During the direct shear test, the normal force was kept constant by horizontal walls #1 and #4, and a shearing load was applied to the sample by moving vertical rigid walls #2 and #3 toward each other at a constant velocity corresponding to a shear strain rate of 0.4%/s. Such a small

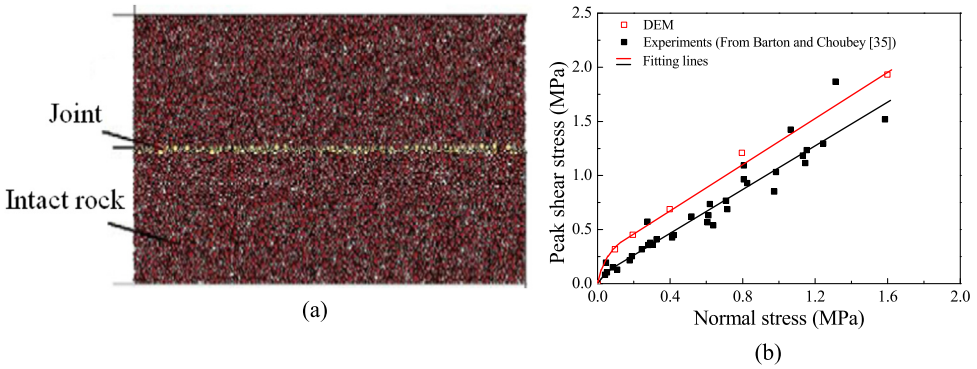

Fig. 7. (a) DEM rock sample with persistent joint and (b) corresponding simulation results compared with laboratory test results [35].

strain rate can ensure that the samples were sheared under quasi-static conditions, which can be judged by the inertial number I calculated by $I = \gamma d\sqrt{\rho_g/P}$, where γ is the strain rate, d is the diameter of the particle, ρ_g is the density of the particle, and P is the confining pressure [34]. The transition between quasi-static regime and the dense flow regime roughly corresponds to $I = 10^{-3}$. By applying the parameters in Table 1, it can be obtained that the calculated value, $I = 2.7 \cdot 10^{-5}$, is much smaller than the critical value.

In this study, this kind of infilled joints is chosen rather than open joints. Infilled joints are often found in field conditions. Because of the limited laboratory tests on jointed rock, especially on non-coplanar joints, the joint setting in this simulation is chosen to model the arrangement as in [7], where cracks are covered with a grease coating, corresponding to joints with clay filling or coating. Open flaw was selected in [5] and [6], and closed flaw is chosen as in [33]. The given setting of joints in this simulation may affect the experimental comparisons. Fig. 7 illustrates the DEM jointed rock sample, and the corresponding simulation results are compared with laboratory test results by Barton and Choubey [35]. It reveals that the simulated peak shear stresses increase near linearly with the same trend as the mean test results, and are within the range of the reported data, even if simulation results are generally larger, and part of the samples in the laboratory are open joint. Therefore, the given setting in this simulation can at least guarantee the consistency between strength properties of simulation and laboratory test results.

4. DEM numerical results

This section will analyze the numerical results obtained from the DEM direct shear tests on rock samples with coplanar and non-coplanar intermittent joints. The effects of joint persistence on shear behavior of rock with coplanar joints and the effects of joint inclination on the shear behavior of rock with non-coplanar joints are examined, with emphasis on the shear stress, bond breakage number, force chains, and failure pattern.

4.1. Coplanar joint

Direct shear tests are simulated on rock samples with two kinds of coplanar joints (i.e. center joint and side joint, shown in Fig. 5) and joint persistence of 0.6, 0.8 and 0.9, respectively.

4.1.1. Shear stress and bond breakage number

The variations of shear stress and broken bond number against shear displacement are similar for rocks with different joint persistence values, so the case when $k = 0.6$ (as illustrated in Fig. 8) is chosen for detailed discussion. There are two failure modes: the tensile–shear–torsional (TST) failure and the compressive–shear–torsional (CST) failure. The shear process of DEM specimens can be divided into four stages:

(1) elastic shearing phase – the shear stress increases almost linearly with no bond breakage as the shear displacement increases;
(2) crack propagation: the shear stress fluctuates until arriving at the peak as the shear displacement increases, and a large number of bonds break with tensile–shear–torsional failures dominating;
(3) the failure of rock bridges: the shear stress quickly drops to a residual value after the peak;
(4) residual phase: the shear stress remains at a relatively low residual value in spite of some fluctuations, and the number of the microscopic bond breakages consistently grows.

Besides, it can be observed that no sharp increase in bond breakage is observed when the biggest shear stress drops, as normally observed in the literature. This may be due to the fact that before the biggest shear stress drop, there exists a first shear stress drop and after that, the shear stress fluctuates. In this stage, the number of bond breakages increases.

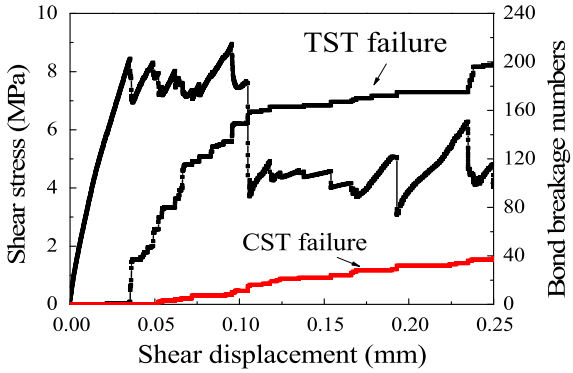

Fig. 8. Variations of shear stress and broken bond number against shear displacement.

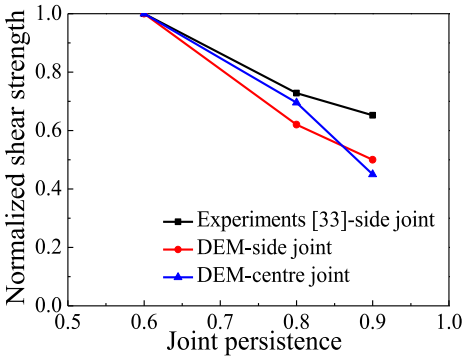

Fig. 9. Relationship between the normalized peak shear stress and the joint persistence obtained from DEM simulation and experiments [33].

Fig. 9 presents the relationships between normalized peak shear stress and joint persistence in DEM simulations and experiments [33]. In the figure, the shear strength in numerical and experimental results is normalized by the peak stress in the case of $k = 0.6$ with normal stress fixed at 1 MPa. Fig. 9 shows that the peak shear stress decreases nearly linearly with the increase of joint persistence, in accordance with the trend of rock samples with persistent joint in the laboratory [33]. There is a qualitative agreement between DEM simulations and experimental data, in spite of the discrepancies of the peak shear stress, and the discrepancies are associated with the distinction of the block test material and the very low friction coefficient. In this, case increasing joint persistence increases the number of particles with zero friction after shear. Thus the difference between the DEM and laboratory tests is more obvious at larger joint persistence.

4.1.2. Force chains

The contact forces recorded at different shear stages of the DEM samples with center and side joint are illustrated in Figs. 10 and 11, respectively. In the figures, the lines are parallel to the directions of contact forces, and the thicknesses of the lines are proportional to the magnitude of the forces. Compressive forces are marked in black, while tensile forces are in red. The purple arrows are added to show the shear direction of each half. Figs. 10(a), (d) and (g) show that, differently from the force chains in the intact sample [36], the compressive forces are concentrated at the edge of the loading plate before the peak shear stress is reached. This phenomenon is typical during direct shear tests [37,38]. The concentration of compressive forces becomes more remarkable when the joint persistence increases as a result of stress concentration near the joint tips. When the shear stress reaches the peak shear stress, and after that, the effects of joint persistence on the force chains are observed in the tensile force distribution. Fig. 10 demonstrates that increasing joint persistence reduces the area of the tensile stress, which can be explained by the fact that larger joint persistence provides more paths for stress to release.

As to the sample with side joint, the effects of joint persistence on the force chains are observed by their distribution and magnitude in the specimens, as illustrated in Fig. 11. When the joint persistence increases, the compressive forces concentrate more obviously near the shear plane and the magnitude of compressive force in the rock bridge decreases. The tensile force decreases with a trend similar to that of the compressive force.

4.1.3. Failure pattern

Figs. 12 and 13 provide the failure patterns of DEM and laboratory specimens, respectively. Figs. 12 and 13 show that the failure patterns of samples with center joint are similar with each other for rocks with different joint persistence. For the failure pattern of the specimen with side joint and $k = 0.6$, the cracks are antisymmetric in the rock bridge with an

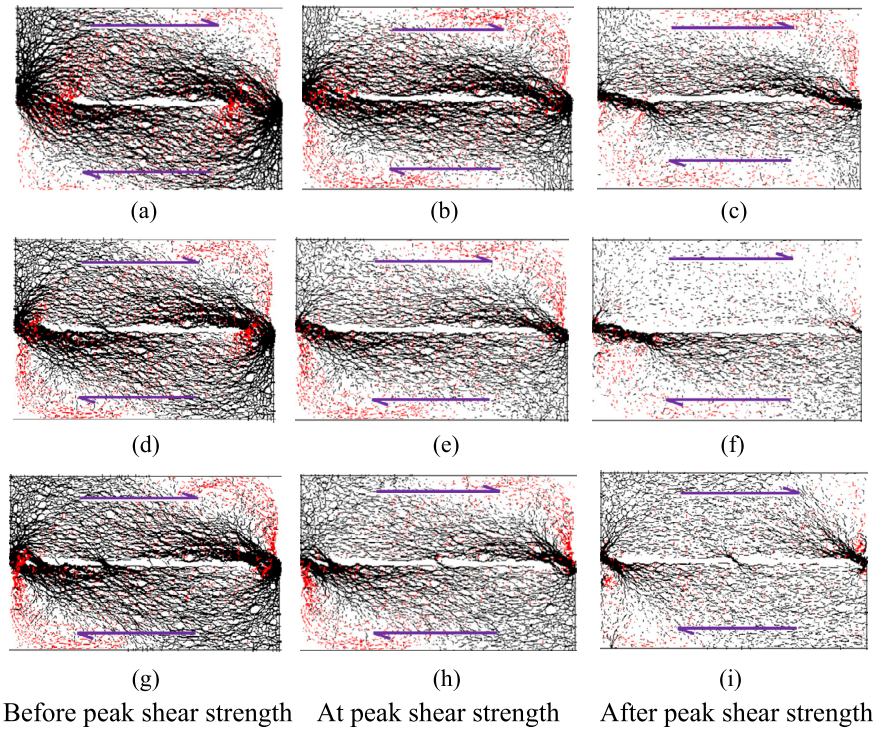

Fig. 10. Force chains in the DEM samples with center joint at different shear stages and for different values of joint persistence: (a–c) $k = 0.6$; (d–f) $k = 0.8$; (g–i) $k = 0.9$.

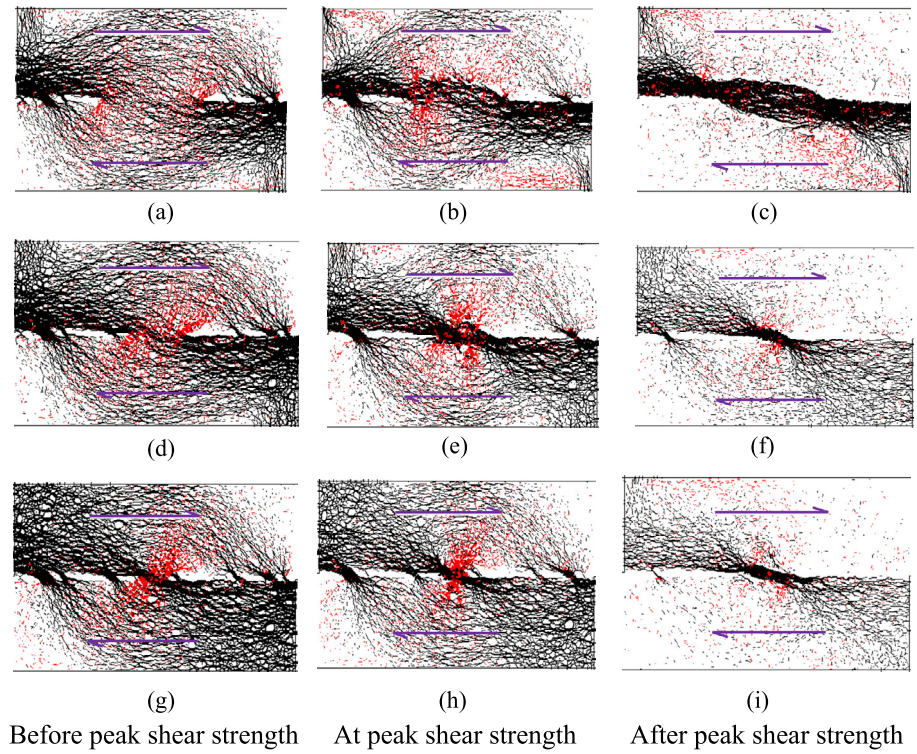

Fig. 11. Force chains in the DEM samples with side joint at different shear stages and for different values of joint persistence: (a–c) $k = 0.6$; (d–f) $k = 0.8$; (g–i) $k = 0.9$.

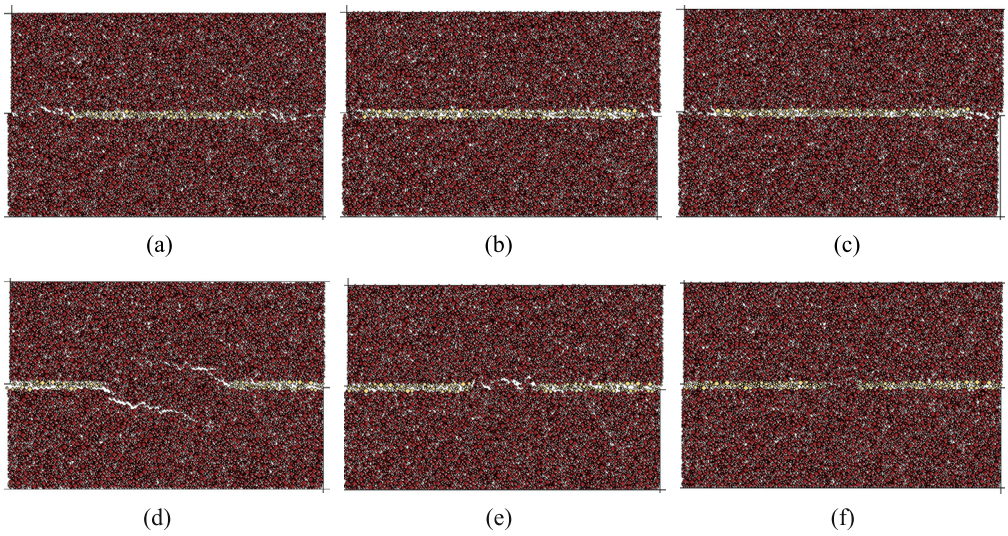

Fig. 12. Failure patterns of the DEM specimens for different joint geometries (a–c: center joints; d–f: side joints) at different persistence values: (a) and (d) $k = 0.6$; (b) and (e) $k = 0.8$; (c) and (f) $k = 0.9$.

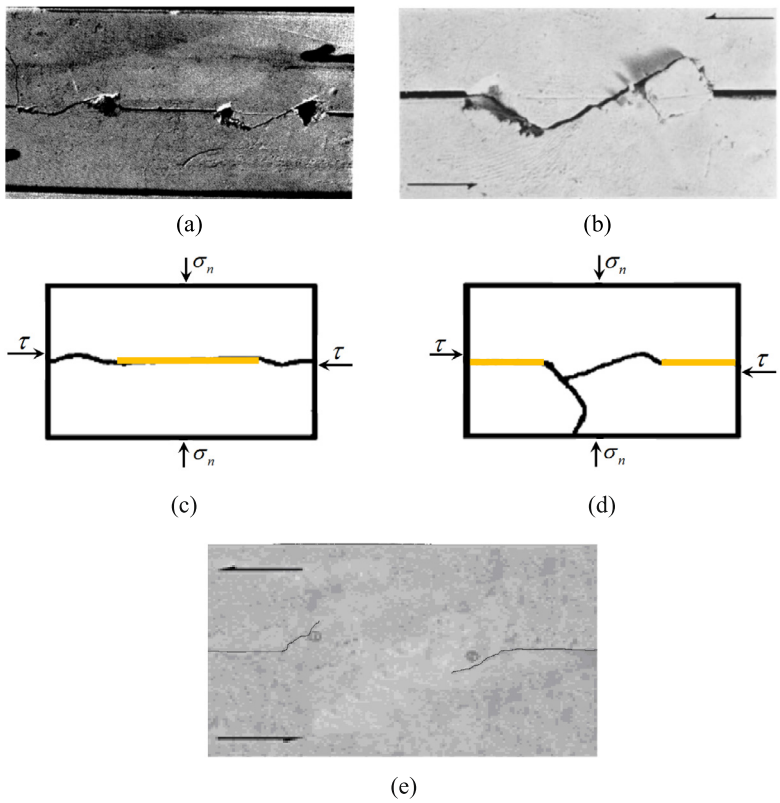

Fig. 13. Failure patterns of the specimens made of (a) and (b) plaster, (c) and (d) plaster and sand mixture and (e) cement mortar in laboratory [5,6,33,39].

inclination of 20° to the shear plane. The cracks in the specimens with $k = 0.8$ and $k = 0.9$ are different, but all of them are parallel to the joints. The difference can be explained by the fact that large joint persistence restricts the area for cracks to develop, which can also induce the stress concentration, as illustrated in Fig. 11. Comparison between Figs. 12 and 13 shows that the failure patterns of the DEM specimens are credible compared to data from laboratory experiments by Lajtai [5,6], Bai et al. [33] and Liu [39]. However, our numerical results miss the completely traversing crack between the two flaws as in Figs. 13(b) and (d), which may be caused by the different rock materials and joint types in the laboratory and the DEM simulation. In experiments, open joint is selected [5,6] and the rock sample is made of gypsum [5,6,33], while our

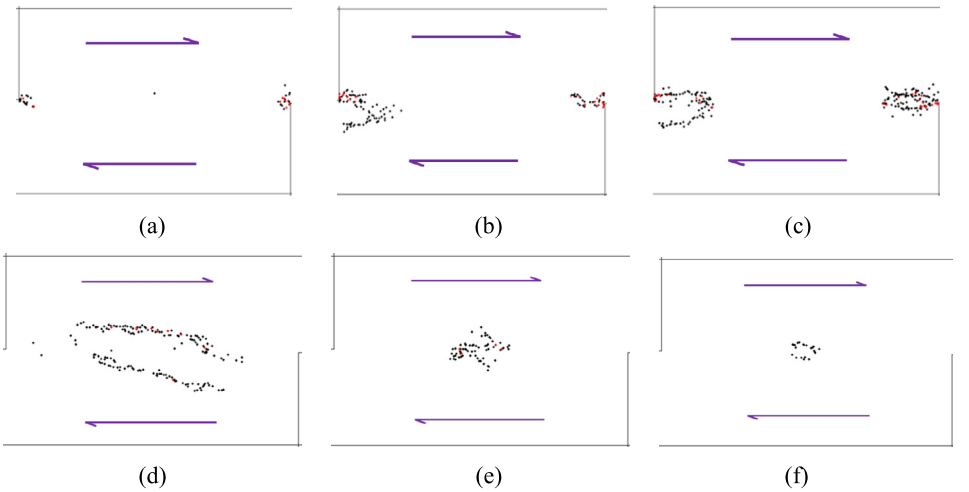

Fig. 14. Bond breakages in the failure samples with: (a)–(c) center joint, (d)–(f) side joint for different joint persistence values: (a) and (d) $k = 0.6$; (b) and (e) $k = 0.8$; (c) and (f) $k = 0.9$.

simulation is more adequate for infilled rock joints and the granite is the target material. In the experiments [39], the rock sample is made of cement mortar, which is more close to the simulated material. Thus the failure patterns in our simulation are more comparable with Fig. 13(e) than with Figs. 13(b) and (d).

As some of the failure patterns in Fig. 12 are not very clear and the bond failures are more convincing in representing the failure of rocks, Fig. 14 presents the bond failures in the DEM specimens, where the black dots represent tension bond failure and red dots represent shear–torsional bond failure. The bond compressive failure is not shown because most of the bond failures are caused by tension and shear–torsion. Fig. 14 shows that in the case of center joint (Figs. 14(a)–(c)), tension bond failures aggregate between the endpoints of the joint. In the case of side joint (Figs. 14(d)–(f)), tension bond failures appear symmetrically at the endpoints of the joint. In both cases, the bond failures are dominated by tension failures.

4.2. Non-coplanar joint

Direct shear tests are simulated on jointed rock samples with different joint inclinations (i.e. 90°, 75°, 60°, 45°, 30°, 15°, 0°, −15°, −30°, −45°, −60° and −75°, respectively), a fixed normal stress of 1 MPa and given parameter l/e of 0.8.

4.2.1. Shear stress and bond breakage number

Fig. 15 illustrates the shear stress–shear displacement relationship and the bond breakage–shear displacement relationship of the DEM samples. Fig. 15 shows that the shear stress versus shear displacement curves are similar to each other in case of different joint inclinations. When i varies from 0° to 90°, the shear stress firstly increases nearly linearly with increasing shear displacement. Shear stress abruptly decreases to the residual shear strength after the peak, and the bond breakage number starts to increase at the maximum increasing rate. Then, shear stress and the bond breakage number remain nearly unchanged regardless of the increase in shear displacement. Comparison of different values of i (Figs. 15(a)–(g)) shows that the peak and residual shear stress increase with the absolute value of joint inclination, which can also be observed in the radar plot of the changes in peak and residual strength against different i, as illustrated in Fig. 16. The peak shear stress increases more regularly than the residual shear strength. Meanwhile, when i increases, the number of cracks caused by TST failure increases while the total number of cracks remains almost the same. When i varies from −75° to −15°, the residual shear strength and cracks number caused by TST failure decrease simultaneously. The changes of the TST/CST failure bond breakage number against different values of i at the peak shear stress and residual stage are illustrated in Fig. 17, in which cusps are observed when $i = \pm 15°$ and 90°. These cusps mean that when i changes between ±15° and 90°, the number of TST/CST failure bond breakages changes abruptly, which may be caused by the stress state (largest shear strength when $i = 90°$ and smallest one when $i = 15°$) in the samples. Again the migration of frictionless particles is responsible for this phenomenon when $i = -15°$.

Since shear strength increases with the absolute value of i and since the changes in shear strength when $i < 0°$ and $i > 0°$ are similar at the same absolute value of i, the changes in shear strength are analyzed with regard to the absolute value of i. The average shear strength increment is different for each range of the absolute value of i (as illustrated in Table 2). When the absolute value of i increases from 15° to 30°, the average shear strength increases the most at 39.0%, while the shear strength increases the least when absolute value of i changes from 45° to 60° and from 75° to 90°. It should be noted that the sample with $i = -75°$ has the largest shear strength (17.7 MPa), whereas the lowest shear strength (7.1 MPa) is observed when $i = 15°$. Therefore, it can be concluded that shear strength increases the most when it arrives at its minimum value and varies little when it is at the maximum value. This can be partly explained by the

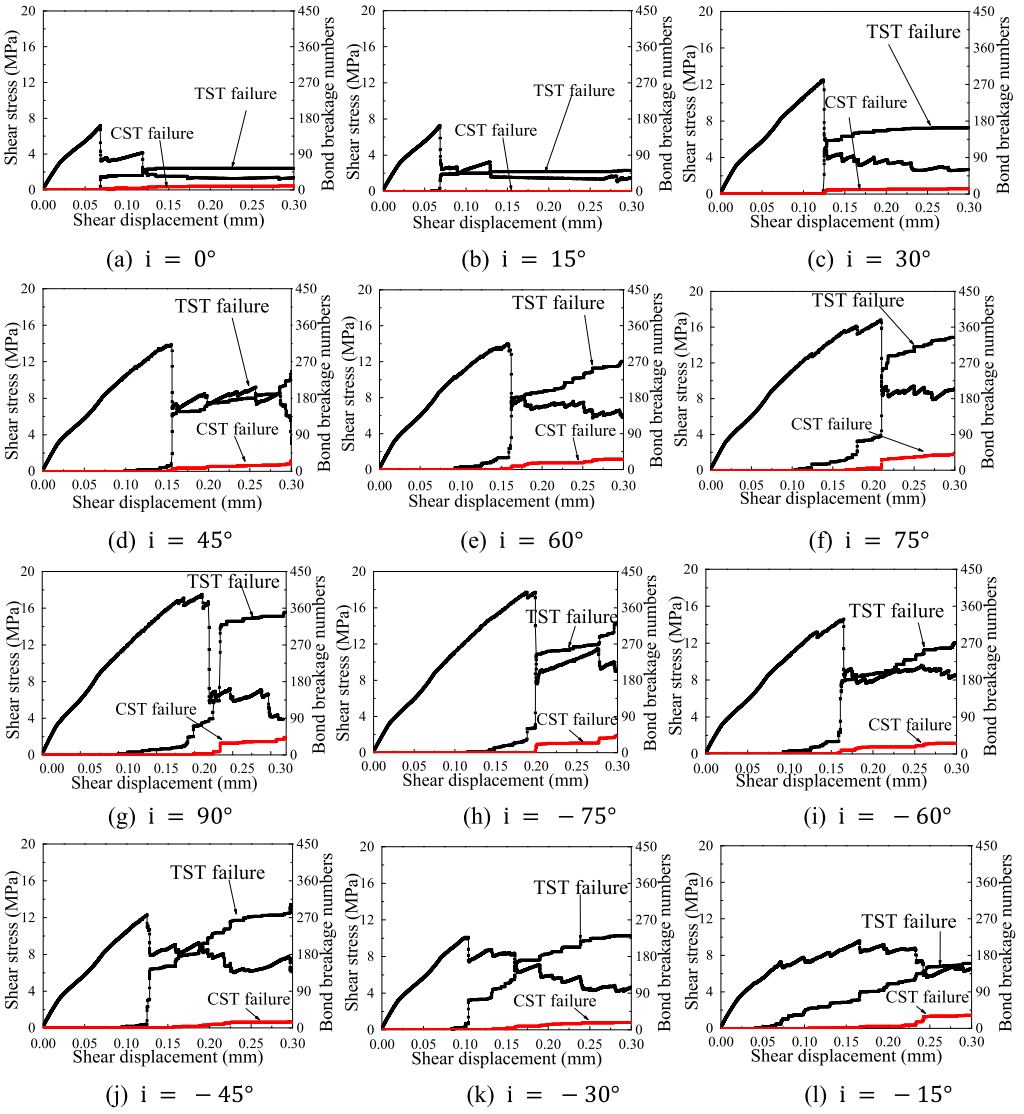

Fig. 15. The shear stress–shear displacement relationship and bond breakage–shear displacement relationship obtained from the DEM sample with different values of *i*.

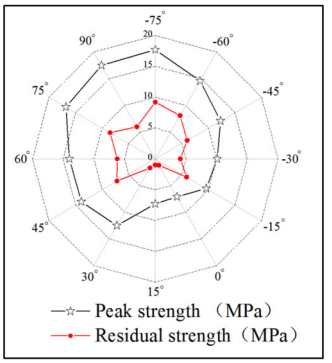

Fig. 16. Changes of peak and residual strength for different joint inclinations.

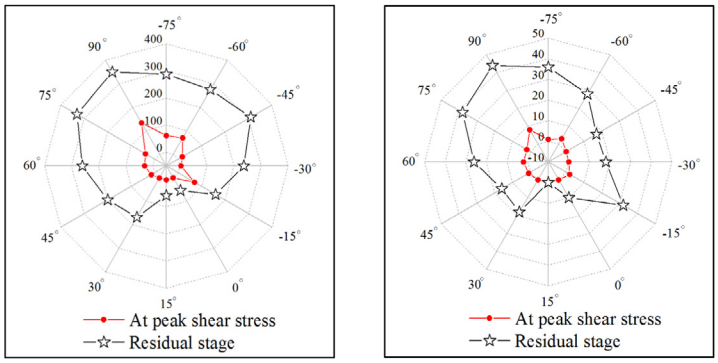

Fig. 17. Changes of (a) TST failure and (b) CST failure bond breakage number against different i at peak shear stress and residual stage.

Table 2
Average increment of shear strength with the absolute value of joint inclination.

Joint inclinations interval (°)	Average increment of shear strength (%)
0–15	18
15–30	39.0
30–45	23.9
45–60	2.9
60–75	20.5
75–90	4.0

distribution of yellow particles (with zero friction and infilling "open" cracks) on the generated shear surface, and will be further discussed with the failure pattern in Fig. 20. However, there are somewhat little changes in the average increment of shear strength when the absolute value of i varies from 45° to 60°. This can be explained by the changes of bond breakages when the peak shear stress has arrived. This is more evident if we observe the change tendency of the peak strength in Fig. 16 and of the TST/CST failure bond breakage number at the peak shear stress in Fig. 17.

4.2.2. Force chains

Fig. 18 illustrates the force chains in the DEM specimens with different values of i when the shear displacement $D_s = 1.5\delta_p$, where the δ_p is the displacement when the maximum shear stress has arrived. Fig. 18 shows that most part of the compressive force chains are located at two or three rock bridges as a result of the coalescence of rock bridges, and the distributions of these force chains are mainly controlled by i, namely the compressive force chains are parallel to the rock bridges. Also, the compressive force chains in the DEM samples with low absolute value of i are narrower than those of the DEM samples with high absolute value of i, and the tensile force chains distribute more widely in the samples with larger absolute value of i. This is because the rock bridges in DEM samples with high absolute value of i are more likely to endure large shear stress. In addition, the sample with $i = 15°$ contains the least compressive force chains at the residual stage, and Fig. 17 shows that both the TST and CST bond failures are the least when $i = 15°$. Therefore, it can be concluded that the bond failures may directly affect force chains distribution.

Typically, the distribution of compressive force chains when $i > 0°$ is obviously different from that in cases when $i < 0°$. For example, the joint is closed and can transfer compressive forces when $i > 0°$, inducing the crack to propagate along the compressive force chain in the rock bridge, and the failure mode is analogous to that in the Brazilian test [7], as illustrated in Fig. 19, whereas, when $i < 0°$, the joint is open and cannot transfer compressive forces, thus the crack cannot propagate across the rock bridge. As a result, the length of the failure of a rock bridge differs under different joint inclinations, and the peak shear stress is also affected, as can be observed in Figs. 16 and 17.

4.2.3. Failure pattern

Fig. 20 presents the failure patterns of the DEM samples with different values of i to analyze the failure patterns of DEM non-coplanar joint samples. Fig. 20 shows that when i varies from 0° to 90°, the cracks are initiated at the endpoint of the joint to the midst of the joint. The breakage of the rock bridge is caused by the coalescence of the cracks from the bottom to the tip of the joint and that from the bottom to the midst part of the joint, and eventually by the coalescence of the cracks from the bottom to the tip of the joint. When i is less than 0°, coalescence of cracks mainly evolves from the bottom to the bottom of joint or from the tip to the tip of the joint. Fig. 21 shows the failure patterns of samples in laboratory [7]. Note that as the loading direction in the laboratory is opposite to that in the simulation, the sign convention of the inclination in laboratory is reversed to insure that the samples in the laboratory and the DEM simulation are comparable for the same i. The comparison between our numerical results and laboratory observations demonstrates that our DEM results are at least

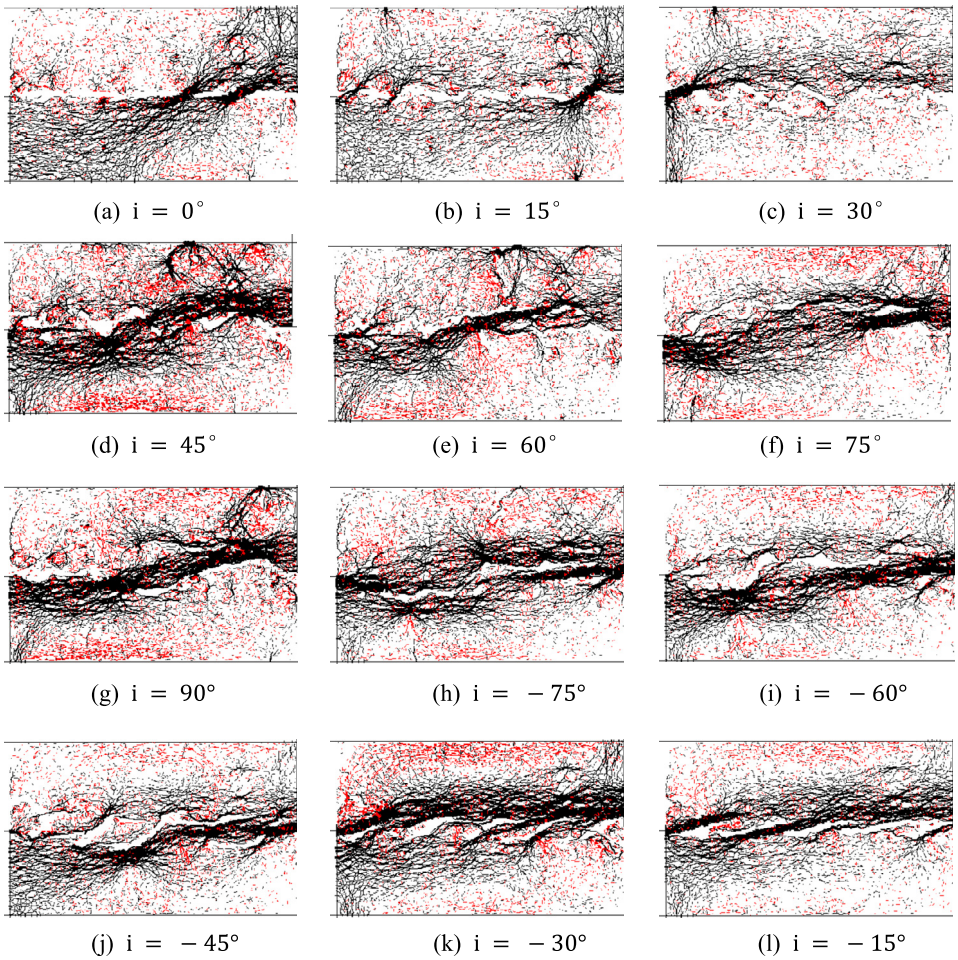

Fig. 18. Force chains in the DEM non-coplanar joint samples with different joint inclinations when $D_s = 1.5\delta_p$.

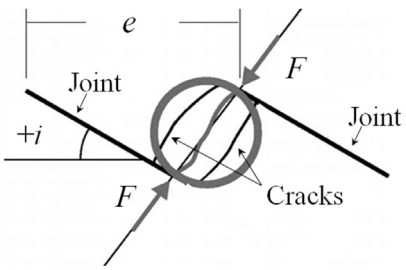

Fig. 19. Failure model of the analogy Brazilian test [7].

qualitatively credible apart from some differences, especially for samples with high inclinations. The differences may be induced by the setting of the joint in the simulation, which actually enhances the friction of joint and the open degree of joint with high inclination is low, and the failure mode of the rock bridge is affected by the compressive force chain near the joint (as illustrated in Fig. 18), which may further affect the peak strength of the sample.

Recalling the average increment of shear capacity with the absolute value of i in Table 2, we can find that the average shear capacity increases the most when i increases from 15° to 30°, while increases it the least when i changes from 45° to 60° and from 75° to 90°. In Fig. 20, some yellow particles (representing the joint) spread over the generated shear surface in the samples with $i = 15°$ and $-15°$, while there is no yellow particle on the generated shear surface in other DEM samples. The yellow particles with zero friction will cause a strong decrease in peak and residual strength, which can explain the variation of shear capacity and the residual strength of rock samples with different i in Fig. 16. Meanwhile, the distinct increment of shear strength (e.g., 39.0% and 2.9%) in Table 2 can be also explained by the migration of the frictionless particles.

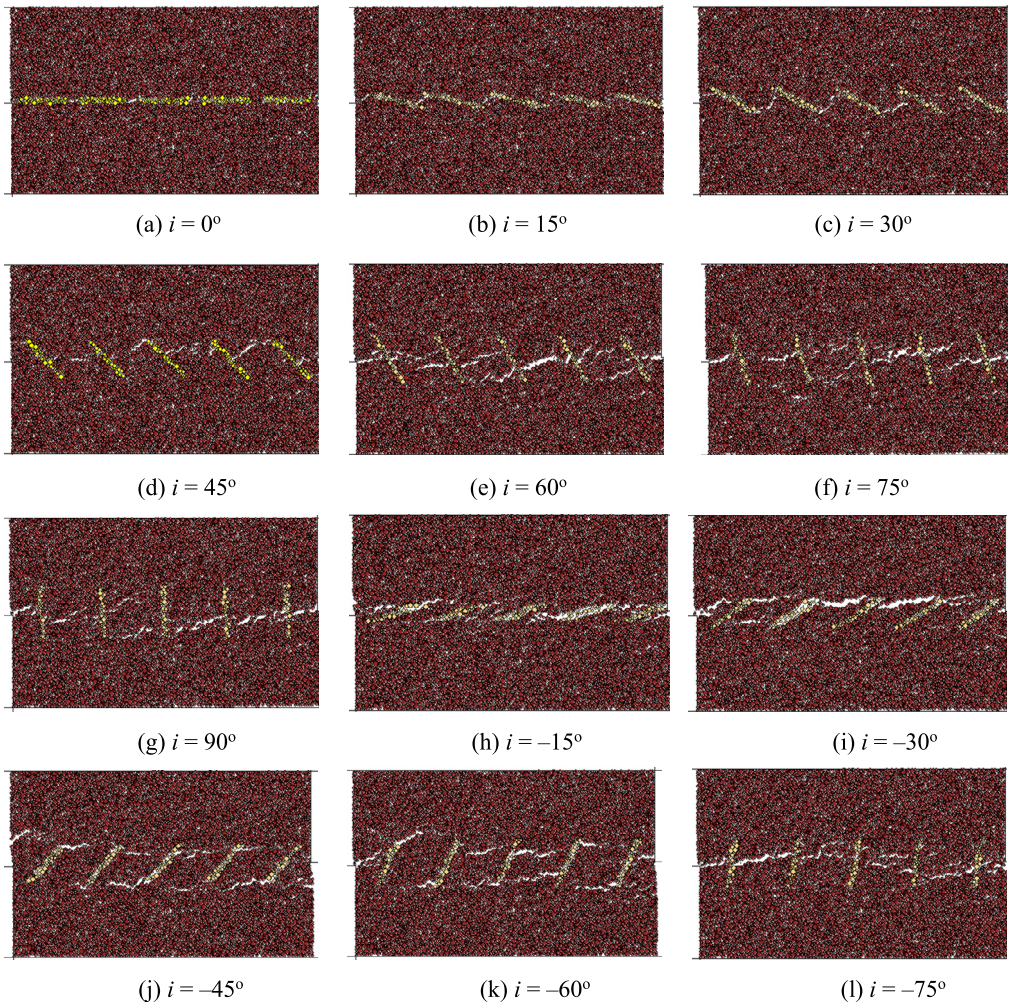

Fig. 20. Failure patterns of DEM non-coplanar joint samples with different joint inclinations.

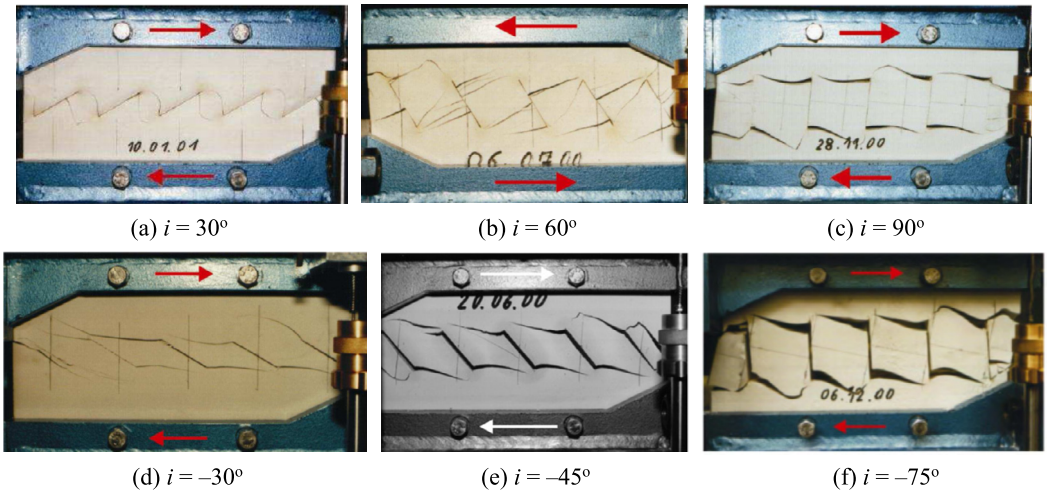

Fig. 21. Failure patterns of samples in laboratory tests [7] performed on pure gypsum (the sign convention for the inclination angle i has been reversed due to the opposite loading directions in laboratory and DEM tests).

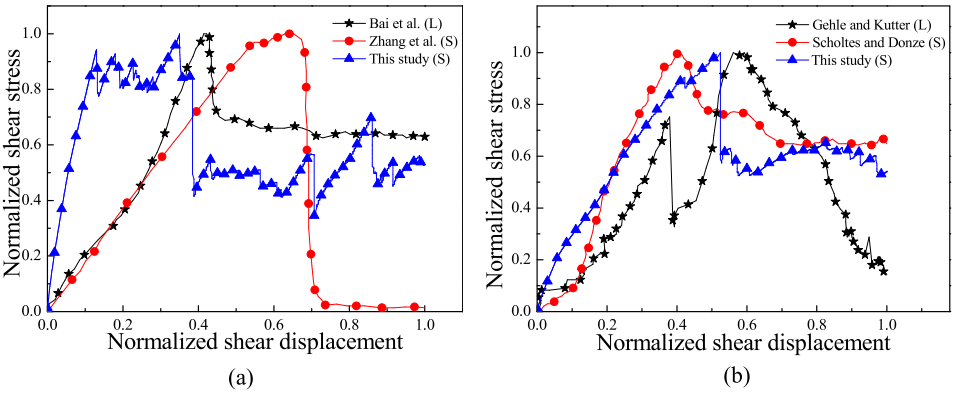

Fig. 22. Comparison on normalized shear stress–displacement relationships between other works [7,13,14,33] and this study: (a) comparison for coplanar jointed rocks; (b) comparison for non-coplanar jointed rocks.

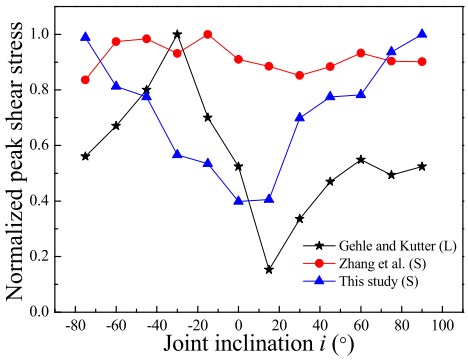

Fig. 23. Relationship between the normalized peak shear stress and i obtained in the laboratory (L) [7], other numerical tests (S) [14], and this study (S).

5. Discussion

Fig. 22 presents several normalized stress–displacement curves for coplanar and non-coplanar (only the case when $i = 45°$ is chosen) jointed rocks under similar test conditions (normal stress, k, i) in the laboratory (L) and in DEM simulations (S). The curves are normalized with respect to their maximum values to qualitatively compare the results in this study and other contributions [7,13,14,33] because of the limited experimental data about the different investigated lithologies. Fig. 22(a) shows that for coplanar jointed rock simulations, as discussed in subsection 4.1.1, shear stress firstly increases nearly linearly with shear displacement, and then fluctuates until the peak stress has arrived. However, no fluctuation is observed in laboratory tests, which can be explained by the different test materials and settings of joints. In the laboratory tests, rock samples are made of plaster and sand mixture (UCS = 14.27 MPa and $E = 4.68$ GPa), and the joints are open, with no infilling. In our simulations, the calibrated material is Lac du Bonnet granite (UCS = 200 MPa and $E = 67.53$ GPa) and joints are filled with frictionless particles. The stress fluctuations might be caused by the frictionless particles migration and the stiffer behavior of the particles within the joints. After the peak, the shear stress drops sharply to a residual value both in the laboratory and in numerical results. Fig. 22(b) shows that for non-coplanar jointed rocks, there are obvious fluctuations in laboratory results after the first peak shear stress has arrived. Then, the shear stress increases again till a higher peak shear stress has arrived, then, in a fashion similar to that of the coplanar jointed sample, the shear stress decreases to a residual value. The fluctuation, however, is not obvious in the numerical results in this study and in [13]. The different test materials (pure gypsum in laboratory and Fontainebleau sandstone by Scholtes and Donze) may be the cause for this difference. Nevertheless, this does not disprove at least the qualitative consistency between numerical and experimental results during the whole shear process.

Fig. 23 illustrates the relationship between the normalized peak shear stress and i obtained from experiment [7], other numerical tests [14], and this study. Fig. 23 shows that this study is more consistent with the experiment than other simulations. In this study, the peak shear stress decreases when i changes from $-75°$ to $15°$, and increases when i changes from $15°$ to $90°$. A similar trend is observed in the laboratory except for the case when i changes from $-75°$ to $-45°$. This difference is probably caused by the different loading and boundary conditions, which induce different failure patterns in Figs. 20 and 21 (e.g., $i = -75°$ and $-45°$, compared in Figs. 20(l) and (j) and Figs. 21(f) and (e)). These figures show that the wing crack propagates from the tip of the joints in laboratory tests, and from the joint centers in this study, which induces a longer rock failure path when $i = -75°$ than $i = -45°$ in our numerical simulations.

6. Conclusions

This paper analyzed the effect of different joint geometries on the failure behavior of rock samples by the DEM incorporating our bond contact model [23]. A series of DEM direct shear tests on rock samples with coplanar and non-coplanar joints was carried out. The numerical results were discussed with emphasis on shear stress, bond breakage number, force chains, and failure pattern. The comparison between the numerical results and experimental data was also made. The main conclusions are as follows:

(1) the failure pattern of jointed rock is greatly affected by joint geometries and the failure of bonds due to tension is the dominant factor leading to the failure of the samples. The migration of frictionless particles can induce a strong decrease of the peak and residual strength;
(2) for samples with coplanar joints, peak shear stress increases when the joint persistence decreases. The shear process includes the elastic shearing phase, crack propagation, the failure of rock bridges, and the residual phase;
(3) the cracks of the coplanar jointed rock are initiated at the end of the shear phase, and the shear plane becomes straighter when the joint persistence is larger. When the joint persistence is low, the wing cracks are long and the waviness of rock bridge failure plane is obvious. The cracks in the failure samples are significantly affected by the joint's persistence;
(4) for rocks with non-coplanar joints, the peak shear stress is positively correlated with the absolute value of joint inclination angle. The shear capacity increases the most when it arrives at its minimum value and varies little when it is at the maximum value. Quantitatively, when i increases from 15° to 30°, the average shear capacity increases the most as 39.0%, while the shear capacity increases the least when i changes from 45° to 60° and from 75° to 90°.

In spite of the differences caused by test materials and boundary conditions, comparison with experimental and numerical results shows that the adopted model is at least qualitatively able to capture the shear behavior of the rock. Besides, our contact model is calibrated for granite, but some numerical results are compared with experimental data obtained from the tests on gypsum. This is because there are few laboratory tests on jointed rock, especially on non-coplanar joints. Moreover, rock fracturing is a 3D process. Therefore a 3D DEM simulation is generally more accurate than a 2D DEM. This is because 2D DEM has its limitations such as inefficiency to capture the volumetric strain behavior of the materials since the particles cannot move spatially into adjacent voids as possibly happening in 3D conditions. However, the 2D DEM in this paper can satisfactorily capture the strength features of rocks, with carefully selected parameters, as well as the material's failure and stability. Therefore the DEM with the new bond contact model is in a position to be applied further to rock mechanics and practical rock engineering problems (e.g., the rock slope), which will be one of our future works.

Acknowledgements

This work is financially supported by the Major Project of the Chinese National Programs for Fundamental Research and Development (973 Program) (No. 2014CB046901), National Natural Science Foundation of China (No. 51639008), and the 111 Project (No. B14017).

References

[1] A. Ghazvinian, V. Sarfarazi, W. Schubert, M. Blumel, A study of the failure mechanism of planar non-persistent open joints using PFC2D, Rock Mech. Rock Eng. 45 (2012) 677–693.
[2] C.A. Tang, W.T. Yang, Y.F. Fu, X.H. Xu, A new approach to numerical method of modelling geological processes and rock engineering problems—continuum to discontinuum and linearity to nonlinearity, Eng. Geol. 49 (1998) 207–214.
[3] Y.H. Hatzor, A.A. Arzi, Y. Zaslavsky, A. Shapira, Dynamic stability analysis of jointed rock slopes using the DDA method: King Herod's Palace, Masada, Israel, Int. J. Rock Mech. Min. Sci. 41 (2004) 813–832.
[4] Y.P. Li, L.Z. Chen, Y.H. Wang, Experimental research on pre-cracked marble under compression, Int. J. Solids Struct. 42 (2005) 2505–2516.
[5] E.Z. Lajtai, Shear strength of weakness planes in rock, Int. J. Rock Mech. Min. Sci. Geomech. Abstr. 6 (1969) 499IN7509–508IN8515.
[6] E.Z. Lajtai, Strength of discontinuous rocks in direct shear, Geotechnique 19 (1969) 218–233.
[7] C. Gehle, H.K. Kutter, Breakage and shear behaviour of intermittent rock joints, Int. J. Rock Mech. Min. Sci. 40 (2003) 687–700.
[8] R.H.C. Wong, W.L. Leung, S.W. Wang, Shear strength studies on rock-like models containing arrayed open joints, in: D. Elsworth, J.P. Tinucci, K.A. Heasley (Eds.), Rock Mechanics in the National Interest, Swets & Zeitlinger Lisse, Leiden, The Netherlands, 2011, pp. 843–849.
[9] P. Cao, T.Y. Liu, C.Z. Pu, H. Lin, Crack propagation and coalescence of brittle rock-like specimens with pre-existing cracks in compression, Eng. Geol. 187 (2015) 113–121.
[10] Z. Moradian, H.H. Einstein, G. Ballivy, Detection of cracking levels in brittle rocks by parametric analysis of the acoustic emission signals, Rock Mech. Rock Eng. 49 (2016) 1–16.
[11] S. Zhang, C.M. Leech, FEM analysis on mixed-mode fracture of CSM-GRP, Eng. Fract. Mech. 23 (1986) 521–535.
[12] J. Dolbow, T. Belytschko, A finite element method for crack growth without remeshing, Int. J. Numer. Methods Eng. 46 (1999) 131–150.
[13] L. Scholtès, F.V. Donzé, Modelling progressive failure in fractured rock masses using a 3D discrete element method, Int. J. Rock Mech. Min. Sci. 52 (2012) 18–30.
[14] H.Q. Zhang, Z.Y. Zhao, C.A. Tang, L. Song, Numerical study of shear behavior of intermittent rock joints with different geometrical parameters, Int. J. Rock Mech. Min. Sci. 43 (2006) 802–816.
[15] P.A. Cundall, O.D. Strack, A discrete numerical model for granular assemblies, Geotechnique 29 (1979) 47–65.
[16] D. Potyondy, P.A. Cundall, A bonded-particle model for rock, Int. J. Rock Mech. Min. Sci. 41 (2004) 1329–1364.

[17] N. Cho, C.D. Martin, D.C. Sego, A clumped particle model for rock, Int. J. Rock Mech. Min. Sci. 44 (2007) 997–1010.
[18] Y.N. Wang, F. Tonon, Modeling Lac du Bonnet granite using a discrete element model, Int. J. Rock Mech. Min. Sci. 46 (2009) 1124–1135.
[19] S.Q. Yang, Y.H. Huang, H.W. Jing, X.R. Liu, Discrete element modeling on fracture coalescence behavior of red sandstone containing two unparallel fissures under uniaxial compression, Eng. Geol. 178 (2014) 28–48.
[20] S.Q. Yang, X.R. Liu, H.W. Jing, Experimental investigation on fracture coalescence behavior of red sandstone containing two unparallel fissures under uniaxial compression, Int. J. Rock Mech. Min. Sci. 63 (2013) 82–92.
[21] X.P. Zhang, L. Wong, Cracking processes in rock-like material containing a single flaw under uniaxial compression: a numerical study based on parallel bonded-particle model approach, Rock Mech. Rock Eng. 45 (2012) 711–737.
[22] X.P. Zhang, L. Wong, Crack initiation, propagation and coalescence in rock-like material containing two flaws: a numerical study based on bonded-particle model approach, Rock Mech. Rock Eng. 46 (2013) 1001–1021.
[23] M.J. Jiang, H. Chen, G.B. Crosta, Numerical modeling of rock mechanical behavior and fracture propagation by a new bond contact model, Int. J. Rock Mech. Min. Sci. 78 (2015) 175–189.
[24] M.J. Jiang, Y.G. Sun, L.Q. Li, H.H. Zhu, Contact behavior of idealized granules bonded in two different interparticle distances: an experimental investigation, Mech. Mater. 55 (2012) 1–15.
[25] M.J. Jiang, Y.G. Sun, Y. Xiao, An experimental investigation on the mechanical behavior between cemented granules, Geotech. Test. J. 35 (2012) 678–690.
[26] M.J. Jiang, H.S. Yu, D. Harris, Bond rolling resistance and its effect on yielding of bonded granulates by DEM analyses, Int. J. Numer. Anal. Methods Geomech. 30 (2006) 723–761.
[27] M.J. Jiang, H.S. Yu, D. Harris, A novel discrete model for granular material incorporating rolling resistance, Comput. Geotech. 32 (2005) 340–357.
[28] C.D. Martin, The Strength of Massive Lac du Bonnet Granite Around Underground Openings, PhD thesis, University of Manitoba, Winnipeg, Canada, 1993, p. 278.
[29] C.D. Martin, N.A. Chandler, The progressive fracture of Lac du Bonnet granite, Int. J. Rock Mech. Min. Sci. Geomech. Abstr. 31 (1994) 643–659.
[30] M.J. Jiang, J.M. Konrad, S. Leroueil, An efficient technique for generating homogeneous specimens for DEM studies, Comput. Geotech. 30 (2003) 579–597.
[31] Y.C. Wang, P. Mora, Modeling wing crack extension: implications for the ingredients of discrete element model, Pure Appl. Geophys. 165 (2008) 609–620.
[32] J.F. Hazzard, R.P. Young, S.C. Maxwell, Micromechanical modeling of cracking and failure in brittle rocks, J. Geophys. Res., Solid Earth 105 (2000) 16683–16697.
[33] S.W. Bai, W.Z. Ren, D.X. Feng, Research on the strength behavior of rock containing coplanar close intermittent joints by direct shear test, Rock Soil Mech. 20 (1999) 10–16.
[34] F. da Cruz, S. Emam, M. Prochnow, J.-N. Roux, F. Chevoir, Rheophysics of dense granular materials: discrete simulation of plane shear flows, Phys. Rev. E 72 (2005) 021309.
[35] N. Barton, V. Choubey, The shear strength of rock joints in theory and practice, Rock Mech. Rock Eng. 10 (1977) 1–54.
[36] N. Cho, C.D. Martin, D.C. Sego, Development of a shear zone in brittle rock subjected to direct shear, Int. J. Rock Mech. Min. Sci. 45 (2008) 1335–1346.
[37] S.H. Liu, Simulating a direct shear box test by DEM, Can. Geotech. J. 43 (2006) 155–168.
[38] L. Zhang, C. Thornton, A numerical examination of the direct shear test, Geotechnique 57 (2007) 343–354.
[39] Y.M. Liu, Study on Failure Model and Strength of Rock Mass Containing Discontinuous Joints in Direct Shear, Ph.D. thesis, Tongji University, Shanghai, China, 2007, p. 152.